Mechanisms of circular defects for shallow trench isolation oxide deposition

Jin Kun Lan, Ying Lang Wang, Chuan-Pu Liu, Chuen Guang Chao, Chyung Ay, Chi Wen Liu, and Yi Lung Cheng

Citation: Journal of Vacuum Science & Technology B **21**, 2098 (2003); doi: 10.1116/1.1609475
View online: http://dx.doi.org/10.1116/1.1609475
View Table of Contents: http://scitation.aip.org/content/avs/journal/jvstb/21/5?ver=pdfcov
Published by the AVS: Science & Technology of Materials, Interfaces, and Processing

Articles you may be interested in
Tungsten diffusion in silicon
J. Appl. Phys. **115**, 013501 (2014); 10.1063/1.4859455

Study of stress in a shallow-trench-isolated Si structure using polarized confocal near-UV Raman microscopy of its cross section
Appl. Phys. Lett. **91**, 241902 (2007); 10.1063/1.2825286

Interfacial stability of an indium tin oxide thin film deposited on Si and Si 0.85 Ge 0.15
J. Appl. Phys. **88**, 3717 (2000); 10.1063/1.1288694

Active corner engineering in the process integration for shallow trench isolation
J. Vac. Sci. Technol. B **18**, 700 (2000); 10.1116/1.591262

Deep-submicron trench profile control using a magnetron enhanced reactive ion etching system for shallow trench isolation
J. Vac. Sci. Technol. A **16**, 1502 (1998); 10.1116/1.581177

Re-register for Table of Content Alerts

Create a profile.

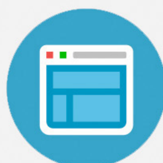

Sign up today!

Redistribution subject to AVS license or copyright; see http://scitation.aip.org/termsconditions. Download to IP: 140.113.38.11 On: Thu, 01 May 2014 05:24:40

Mechanisms of circular defects for shallow trench isolation oxide deposition

Jin Kun Lan
Department of Material Science and Engineering, National Chiao-Tung University, Hsin-Chu, Taiwan and Taiwan Semiconductor Manufacturing Co., Ltd., Hsinchu, Republic of China

Ying Lang Wang[a)]
Taiwan Semiconductor Manufacturing Co., Ltd., Hsinchu, Republic of China and Department of Applied Physics, National Chia Yi University, Chia Yi 600, Taiwan, Republic of China

Chuan-Pu Liu
Department of Materials Science and Engineering, National Cheng Kung University, Tainan, Taiwan

Chuen Guang Chao
Department of Material Science and Engineering, National Chiao-Tung University, Hsin-Chu, Taiwan

Chyung Ay
Department of Biomechatronic Engineering, National Chia Yi University, Chia Yi 600, Taiwan, Republic of China

Chi Wen Liu
Taiwan Semiconductor Manufacturing Co., Ltd., Hsinchu, Republic of China

Yi Lung Cheng
Department of Material Science and Engineering, National Chiao-Tung University, Hsin-Chu, Taiwan and Taiwan Semiconductor Manufacturing Co., Ltd., Hsinchu, Republic of China

(Received 18 November 2002; accepted 21 July 2003; published 15 September 2003)

Shallow trench isolation (STI) is extensively used as the isolation method beyond 0.18 μm generation. This study explored the formation of circular defects in high-density plasma (HDP) STI deposition. Circular defects were caused by the burst flow of silane reactive gas. The defect maps were coincident with the silane flow field. Fourier transform infrared and secondary-ion-mass spectroscopy data exhibited that the silane-burst flow formed a silicon rich oxide (SRO) film. This SRO film existed between the STI oxide and liner oxide. The circular defects were easily found using optical microscopy (OM) for STI with SRO film. Scanning electron microscopy and transmission electron microscopy photographs show that these defects include bubbles and concavities. When SRO fully covers the liner oxide, bubbles easily form by delamination between SRO film and liner oxide. This correlates with the high tensile stress produced by the SRO film. Besides this, higher STI deposition temperatures yield more bubbles. When SRO discontinuously forms on the liner oxide, the concavities were induced by the variation of STI deposition rate on SRO film and liner oxide. The surface charge difference between the SRO film and the liner oxide is the driving force for the generation of concavities. © *2003 American Vacuum Society.*
[DOI: 10.1116/1.1609475]

I. INTRODUCTION

The local oxidation of silicon (LOCOS) isolation technique has been used for many years for integrated circuits. Lateral encroachment, also known as bird's beak, is the key disadvantage of this technique, which makes this technique unsuitable for deep submicrometer devices.[1–4] In ultralarge-scale integration (ULSI), there is more need to reduce the size of the isolation region; thus the shallow trench isolation (STI) process has been developed.[5–10]

Recently, high-density plasma (HDP) based chemical vapor deposition (CVD) oxide has been extensively used as a trench filling material because of its good characteristics such as good gap-fill, low thermal budget, low HF-etching rate, and high throughput.[11–14] However, there are still many issues in the STI process, such as planarization improvement,[15,16] corner shape effects,[17] and process-related defect elimination.[18]

Investigations on the improvement of STI planarization after chemical-mechanical polish (CMP) have been addressed.[15,16,19–21] A common solution is the implementation of dummy active area regions. These dummy areas are designed in a way such that the local density of active areas over the chip and over the wafer is rather uniform. In that way, the CMP process can be optimized so that dishing is minimized while keeping the nitride erosion to a minimum.

STI corner shape improvement has also been extensively studied.[17,22–24] A sharp active corner at the STI edge can lead to a high fringing electric field, which can establish a parasitic transistor with a lower threshold voltage (V_t) along the

[a)]Author to whom correspondence should be addressed; electronic mail: ylwang@tsmc.com.tw

Redistribution subject to AVS license or copyright; see http://scitation.aip.org/termsconditions. Download to IP: 140.113.38.11 On: Thu, 01 May 2014 05:24:40

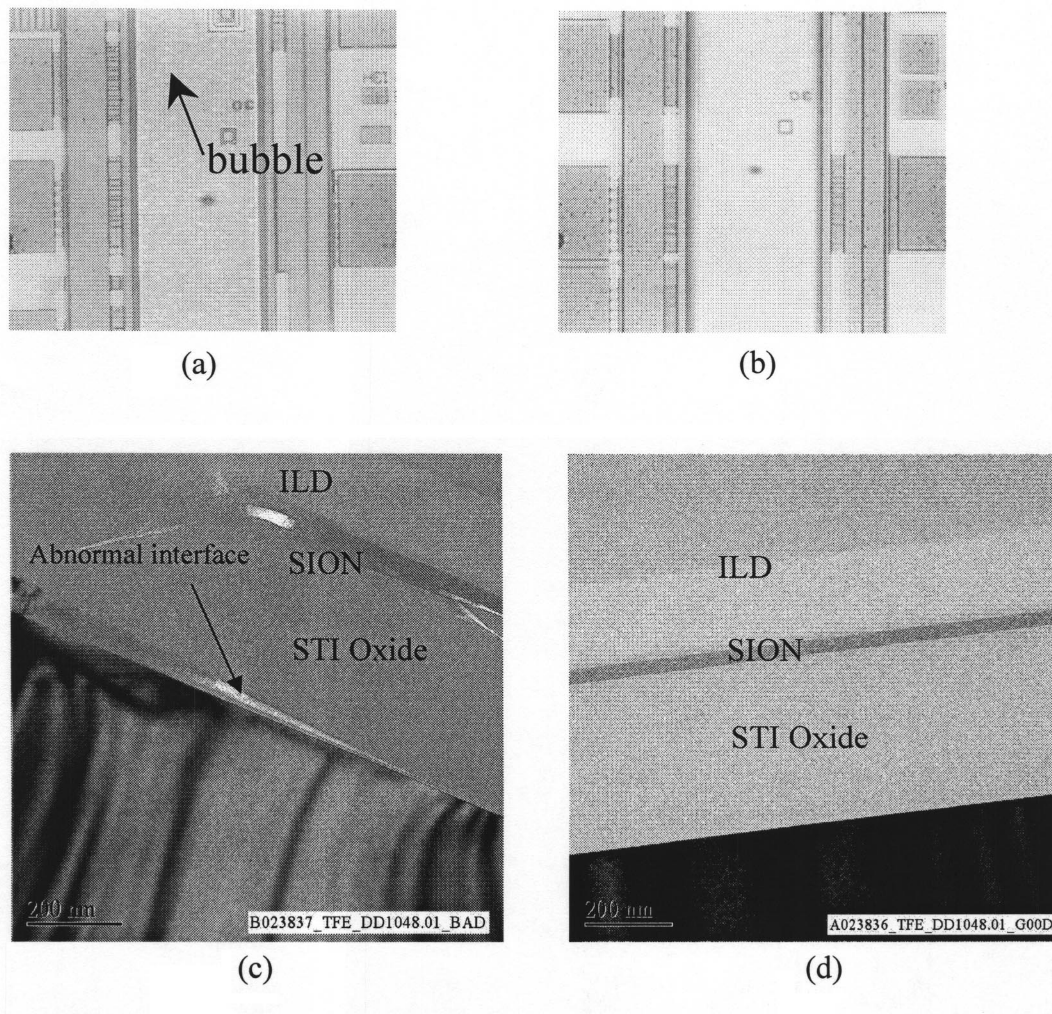

FIG. 1. Photographs of bubble defect on pattern wafers: (a) OM (× 50) with bubble; (b) OM (× 50) without bubble; (c) TEM for the bubble defect; and (d) TEM for normal STI area.

trench edge parallel to the normal transistor.[17] An edge transistor with a lower V_t provides a leakage path even before the normal transistor is turned "on." One of the easily manufacturable remedies is the undercutting of the pad oxide beneath the masking nitride by an isotropic wet etching before the trench liner oxide is grown. Another corner shape issue is the oxide recess at the upper corner of the trench edge that is belived to cause the subthreshold "kink." Many novel STI processes can solve the issue.[22–24]

Most STI defects studied were stress-related. The effects of the stress, induced by the STI process, on the device performance such as data retention time and junction leakage have been explored.[14,25–33] The stress-induced defects examined thus found are dislocations.[25,26,28,32] When STI dislocations are located within the depletion region of the *pn* junction, anomalous junction leakage current could flow. The crystal defects and the mechanical stress are reduced by optimizing the implantation conditions and the densification temperature of trench filled high-density plasma (HDP) oxide, respectively.[25] Many researchers have proposed models and methods to measure and reduce the stress.[34–36]

However, the bubble-like defects in the STI process have seldom been addressed. This investigation considers the circular defects found in the STI process. Scanning electron microscopy (SEM) and transmission electron microscopy (TEM) photographs presented that the circular defects were bubbles and concavities. The mechanisms for the circular defects formation were presented.

II. EXPERIMENT

All wafers used in this study were 200 mm *p*-type (100) Si wafers with resistivity 8–12 Ω cm. Wafers were cleaned with industrial standard clean-1 and clean-2 before the STI process. For patterned wafers, thermal 5 nm oxide layers (pad oxide) were grown atop precleaned Si substrates followed by 160 nm silicon nitride (pad nitride) deposition in a low-pressure chemical vapor deposition diffusion furnace. These stacks were then patterned using a deep ultraviolet lithography system with 0.18 μm feature size for trench formation. After trench etching, thermal 20 nm dry oxide were grown followed by a high-density plasma (HDP) oxide depo-

Redistribution subject to AVS license or copyright; see http://scitation.aip.org/termsconditions. Download to IP: 140.113.38.11 On: Thu, 01 May 2014 05:24:40

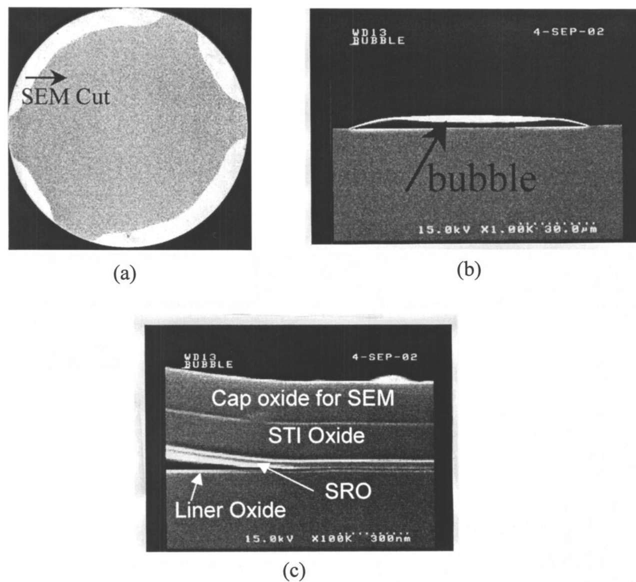

FIG. 2. Photographs of bubble defect on blanket wafers: (a) bubble distribution within the wafer; (b) SEM (× 1 K) image of the defect; and (c) SEM (× 100 K) image of the defect.

sition to fill the trenches. The commercially available Applied Material Ultima Plus@ chamber was used for the HDP oxide. The process parameters for HDP oxide were 1300 W top-rf, 3100 W side-rf, 3000 W bias-rf, 125 sccm argon (Ar), 270 sccm oxygen (O_2), and 140 sccm silane. For blanket wafers, the pad oxide, pad nitride, trench photo and etch steps were skipped. The silane burst film was simulated with films deposited at 110 sccm Ar, 35 sccm silane, 1000 W top-rf, and 2500 W side-rf. The process parameters for Ar sputter rate were 1300 W top-rf, 3100 W side-rf, 3000 W bias-rf, 125 sccm Ar, and 270 sccm O_2. The Applied Material Mirra system was used for the STI chemical-mechanical polish (CMP) process.

The film stress was measured using TENCOR FLX-5400. The contact angle was measured using KYOWA FACE CA-W200 with a 10 μl deionized water droplet for test. The surface charge on the different films was measured using KLA&TENCOR QUANTOX@. The breakdown voltage was measured using a mercury probe by SSM 5100CV system. The criteria for film breakdown was leakage current larger than 10^{-4} A. The Fourier transform infrared (FTIR) was measured using ACCENT QS2000. The secondary-ion-mass spectroscopy (SIMS) was analyzed using CAMECA 6f.

III. RESULTS AND DISCUSSION

A. Bubble defects

Figure 1 displayed the optical microscope (OM) and TEM photographs of the bubble defects in pattern wafers. The TEM photographs exhibited that the bubble was formed by the delamination between STI oxide and furnace liner oxide. Besides, there existed a thin layer of oxide between STI and liner oxide. The simulation for the bubble formation was done on the blanket wafers. An additional step was inserted

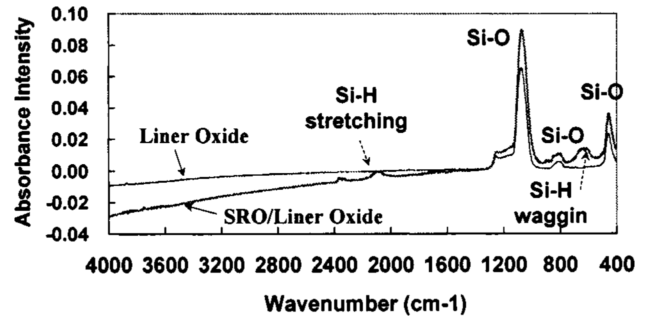

FIG. 3. FTIR peaks for the silane burst film and the liner oxide.

in the STI oxide deposition process. This step was used to enhance the silane burst situation, which easily happened when the mass flow controller (MFC) of silane malfunctioned. When the MFC of silane malfunctioned, silane reactive gas would flow into the reactive chamber before it was set to flow. The SEM photographs of the STI oxide with predeposited silane burst films are presented in Fig. 2. The SEM sample was coated with a compressive tetraethylorthosilicate (TEOS) oxide to prevent damages on the defects when doing the SEM cut. The dark image shown in Fig. 2(a) was the abnormal area. The image pattern correlated well to the silane gas flow field. Figure 2(b) presented that the dark area shown in Fig. 2(a) was a bubble. Figure 2(c) revealed that the bubble originated from the peeling between silane burst film and liner oxide. This phenomenon was equivalent to the defect shown in Fig. 1.

Figure 3 plotted the FTIR peaks of the enhanced silane burst film. The silane burst film contained the Si–H stretching (2100 cm^{-1}) and Si–H wagging (650 cm^{-1}) bonds. Figure 4 presents the SIMS data of the film stacks with STI oxide, silane burst, liner, and Si substrate from left to right. From the FTIR and SIMS data, the silane burst film was silicon-like (SRO) film containing Si–H bonding.

B. Concavity defects

Figure 5 displayed the optical microscope (OM) and SEM photographs of the concavity defects. The SEM sample was coated with a compressive TEOS oxide to prevent damages to the defects when doing a SEM cut. The OM photographs shown in Fig. 5(a) look like the bubble defect displayed in Fig. 1(a); both were circular. Figures 5(b)–5(d) exhibited that the concavity was formed by two steps. First, the dis-

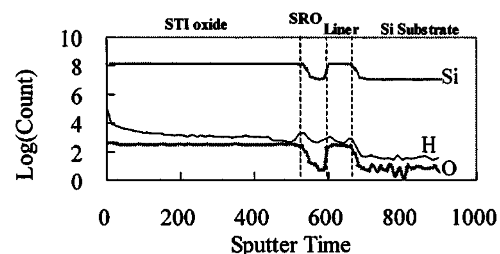

FIG. 4. SIMS analysis for a film stack: STI oxide/SRO film/ liner oxide/Si substrate (from top to bottom).

Redistribution subject to AVS license or copyright; see http://scitation.aip.org/termsconditions. Download to IP: 140.113.38.11 On: Thu, 01 May 2014 05:24:40

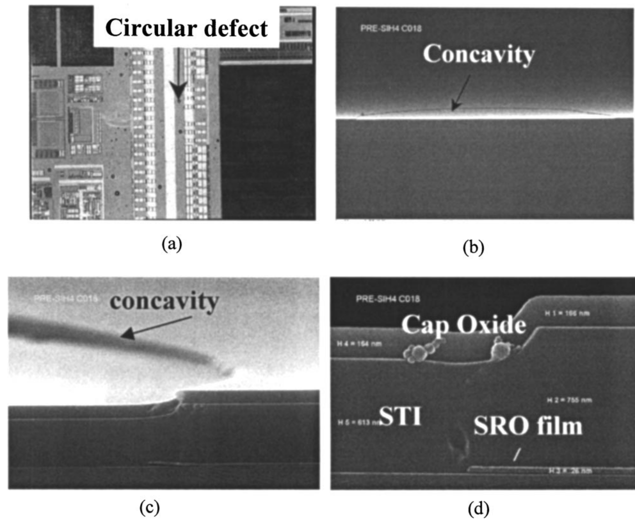

FIG. 5. Photographs of concavity defect on pattern wafers: (a) OM (× 50); (b) SEM (× 1 K) image of the concavity; (c) SEM (× 25 K) image of the concavity; and (d) SEM (× 60 K) image of the concavity.

continuity of SRO film was formed. Second, the difference of STI oxide deposition rate on SRO film and furnace liner oxide magnified the discontinuity. Figure 5(d) yielded that the deposition rate of STI oxide on SRO film was 17% higher than that on liner oxide. The simulation for the concavity formation using the blanket wafers is presented in Fig. 6. Figures 6(a) and 6(b), respectively, present the defect images before and after STI CMP. Figure 6(b) reveals that the bubble-like defects actually represent a discontinuous film, not bubbles, after CMP. This phenomenon matched with the results in the pattern wafer.

C. Mechanism for bubble defect

Figures 1 and 2 revealed that the STI bubble originated from the delamination between SRO films and liner oxide. Table I displays the stress data and contact angle for various films; SRO films had high tensile stress. The difference of the contact angle between STI oxide and liner oxide was 5°. But the difference between SRO film and liner oxide was 9°. This revealed that the adhesion between SRO film and liner oxide was poorer than that between STI oxide and liner oxide. Therefore SRO film made the bubble easily happen. Figure 7 presents the mechanism for bubble formation caused by the tensile stress field and the poor adhesion of SRO film

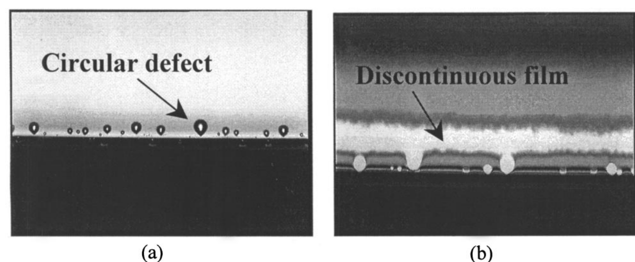

FIG. 6. Photographs of concavity defect on blanket wafers: (a) before STI CMP (× 50); and (b) after STI CMP (× 50).

TABLE I. Stress data and contact angle for various films.

Film	Thickness (nm)	stress (10^9, dyne/cm^2)[a]	Contact angle (degree)
Furnace liner oxide	20	−3.93	33
Silane burst (SRO) film	26[b]	+1.22	24
STI oxide	580	−2.12	28

[a]Negative and positive values presented compressive and tensile stress, respectively.
[b]The thickness of silane burst film was measured using SEM.

with the liner oxide. Detailed stress calculations were possible using finite element techniques, but it was possible to understand how they arose using the following arguments. The temperature profiles produced in the SRO films could be clarified by simple estimates of the quantities in the time-dependent heat conduction equation

$$\frac{\partial T}{\partial t} = \frac{k}{\rho C} \nabla^2 T + \frac{Q}{\rho C}(r,t), \tag{1}$$

where T is the temperature, ρ the density, k the thermal conductivity, C the heat capacity, and Q the heat. In the high-density plasma deposition, argon and reactive species would bombard the SRO surface. The temperature at the SRO surface was higher than that in the SRO–liner oxide interface. The higher temperatures on the external surface caused these to expand more than the inner surface and a bubble resulted. Assuming the deformation was elastic, the elastic energy of SRO was given by[37]

$$U_B \cong EW^3 H^2/R^2, \tag{2}$$

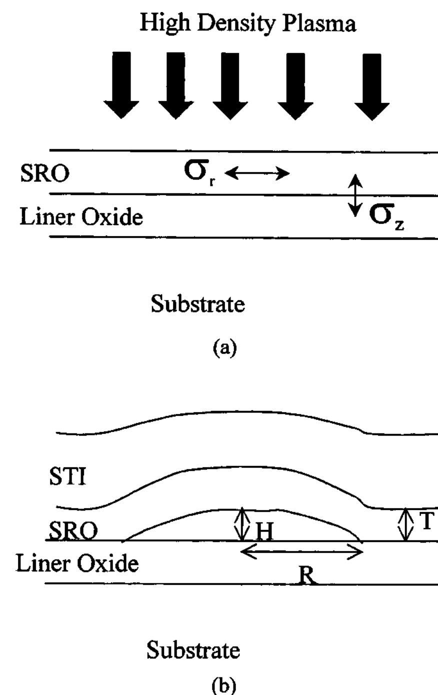

FIG. 7. Mechanism of bubble defect formation: (a) thermal stress distribution and (b) the resulting bubble after STI deposition.

Redistribution subject to AVS license or copyright; see http://scitation.aip.org/termsconditions. Download to IP: 140.113.38.11 On: Thu, 01 May 2014 05:24:40

TABLE II. Bubble extent on blanket wafers for different process conditions.

Condition	With (Y)/without (N)		
Silane burst	N	Y	Y
Low temperature STI deposition	N	Y	N
High temperature STI deposition	Y	N	Y
Bubble (No, Low, High)	No	Low	High

where E is the SRO modulus, W the SRO thickness, R the bubble radius, and H the deflection.

The energy required for the free surface formation was

$$U_S \cong G_c R^2, \tag{3}$$

where G_c is the bulk toughness of liner oxide.
For a stable bubble,

$$\frac{d}{dr}(U_B + U_S) = 0. \tag{4}$$

Hence we may obtain the stable bubble geometry as a function of the material properties from Eq. (4) so that, for a given height H, the bubble radius is given by

$$R \cong (EW^3 H^2 / G_c)^{1/4}. \tag{5}$$

Table II presents the bubble defects on blanket wafers for different process conditions. For no SRO film condition, there was no bubble defect even when STI oxide deposited in high temperature. With SRO film, when the deposition temperature of STI oxide raised, the bubble defect counts increased. These results confirmed that the bubble defect was thermal-stress induced and silane burst was the important factor.

D. Mechanism for concavity defect

Figures 5 and 6 revealed that the STI concavity happened because of the discontinuity of SRO films and the surface sensitivity of STI oxide on different substrate, i.e., SRO films and liner oxide. The electrostatic effects on the surface related phenomena have been addressed for the semiatmospheric chemical vapor deposition (SACVD) process.[38] However, the same effect has never been presented for HDP STI deposition. Table III displays the surface charge, the STI deposition rate (DR), and argon sputter rate (SR) on various films. The surface charge on SRO film was higher than that on liner oxide. However, Table III reveals that the surface effects on the STI oxide DR and argon SR are unclear. However, Fig. 5 clearly shows that the concavity was formed across SRO and liner oxide. We propose that it was the charge difference, not charge, acting as the driving force to cause the surface sensitivity of STI oxide. The positive argon ions (Ar^+) were known as the species for sputter-etching in the HDP oxide deposition process. There were two kinds of processes in HDP deposition which were deposition and *in situ* sputter-etching. The SRO films had positive potential and liner oxide had negative potential. The sputter-etching over the SRO films was reduced and the deposition process was enhanced. This enhancement lead to the concavities. Figure 8 presents the mechanism for the formation of concavity. The potential V generated by the charge difference between SRO and liner oxide lead to the different deposition rate of STI on SRO and liner oxide. Figure 5(d) displays that the step height between liner oxide and SRO film was 26 nm before STI oxide deposition. But, after depositing 613 nm STI oxide, the step height increased to 142 nm. This high

TABLE III. Surface charge, the STI deposition rate, and argon sputter rate on various films.

Film	Surface charge (V)	STI D.R.(nm/min)[a]	Ar S. R.(nm/min)[b]
Liner oxide	−0.3	703.6	131.8
Silane burst (SRO) film	+5.5	705.9	134.7

[a]STI D.R.: STI oxide deposition rate.
[b]Ar S.R.: argon sputter rate, using the STI D.R. wafers to measure the sputter rate.

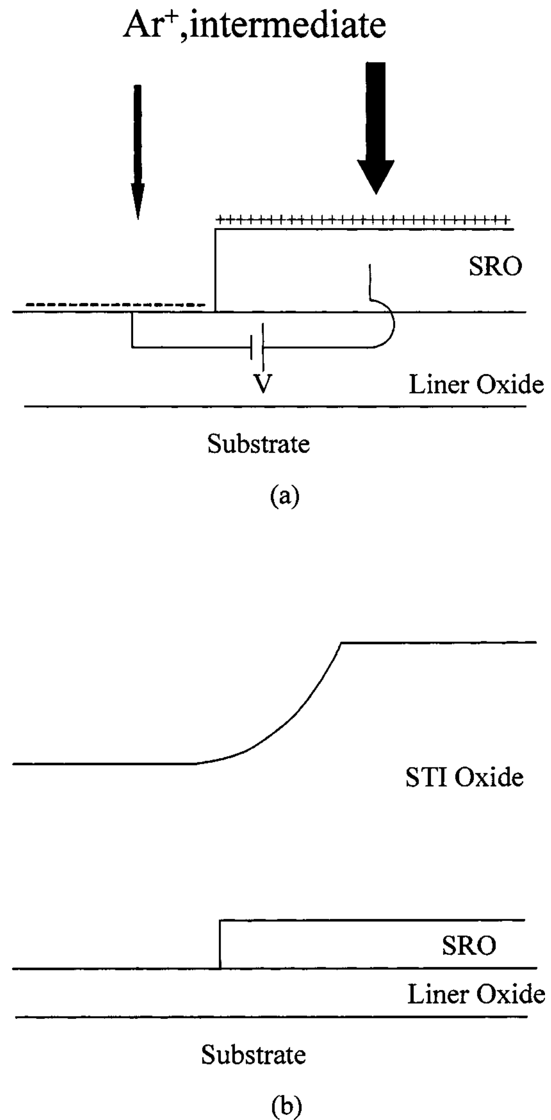

FIG. 8. Mechanism of the concavity defect formation: (a) the charge distribution and (b) the resulting concavity after STI deposition.

Redistribution subject to AVS license or copyright; see http://scitation.aip.org/termsconditions. Download to IP: 140.113.38.11 On: Thu, 01 May 2014 05:24:40

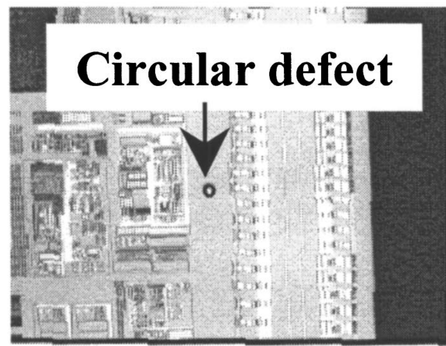

(a)

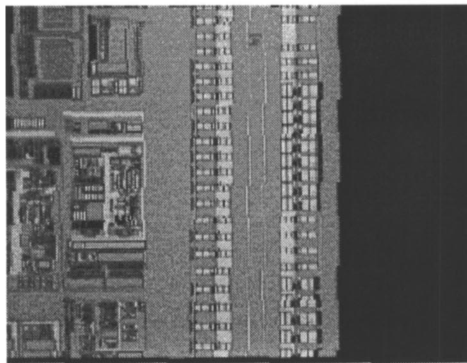

(b)

FIG. 9. Photographs of circular defects for different liner conditions: (a) furnace oxide liner only; and (b) bilayer liner: SiON atop of furnace oxide liner.

step made the concavity easily observed using OM. The circular shape of the concavity correlated to the poor wetting ability of liner oxide for the deposition of SRO film. Therefore these results verified that the concavity defect was SRO film-induced.

SiON film has been studied to replace furnace oxide as the liner material.[22] We found that the bilayer liner, SiON atop of oxide, reduced the circular defects. Figure 9 presents that the film stack with a bilayer liner showed no circular defect. Besides, the bilayer liner also improved the STI strength. The breakdown voltage of STI is displayed in Fig. 10. The breakdown voltage using a bilayer liner was near twice of that using an oxide liner only. The mechanism for the improvement of SiON on STI defects needs further study.

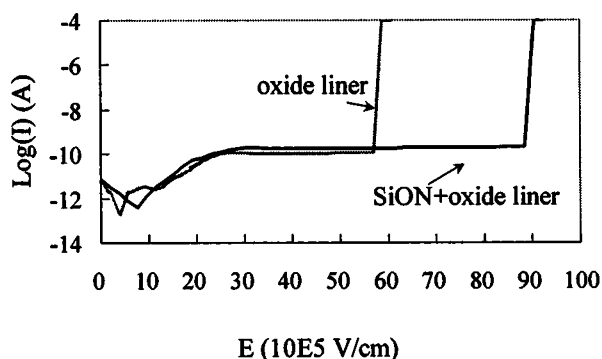

FIG. 10. $I-V$ curve for different liner conditions.

IV. CONCLUSIONS

Circular defects were found in the high-density plasma (HDP) STI deposition process. SEM and TEM photographs presented that these defects were bubbles and concavities. The distributions of these defects matched with the flow field of silane. With the enhanced-duplication of silane burst flow, the circular defects were generated. FTIR and SIMS data exhibited that the burst flow of silane formed a thin silicon-like (SRO) film. This SRO film existed between the STI and liner oxide and had high tensile stress. When SRO film fully covered the liner oxide, bubbles formed because the contact angle data revealed that the adhesion between SRO and liner oxide was poorer than that between STI and liner oxide. The bubble was thermal-stress induced and SRO film was the key factor. When SRO film was discontinuous, the concavity was generated. The concavity was caused by the variation of STI deposition rate on SRO film and liner oxide. The difference in STI deposition rate was caused by charge potential, which was generated by the different surface charge.

[1]J. A. Appels, E. Kooi, M. M. Paffen, J. J. H. Schatorje, and W. H. C. G. Verkuylen, Philips Res. Rep. **25**, 118 (1970).
[2]J. W. Lutze and J. P. Krusius, IEEE Trans. Electron Devices **ED-38**, 242 (1991).
[3]S. S. Roth, W. J. Ray, C. Mazure, K. Cooper, H. C. Hirsch, C. D. Gunderson, and J. Ko, IEEE Trans. Electron Devices **ED-39**, 1085 (1992).
[4]K. Blumenstock, J. Theisen, P. Pan, J. Dulak, A. Ticknor, and T. Sandwick, J. Vac. Sci. Technol. B **12**, 54 (1994).
[5]K. Shiozawa, T. Oishi, H. Maeda, T. Murakami, K. Yasumura, Y. Abe, and Y. Tokuda, J. Electrochem. Soc. **145**, 1684 (1998).
[6]K. Shiozawa, T. Oishi, K. Sugihara, A. Furukawa, Y. Abe, and Y. Tokuda, Jpn. J. Appl. Phys., Part 2 **38**, L234 (1999).
[7]M. Bohr, S. U. Ahmed, L. Brigham, R. Chau, R. Gasser, R. Green, W. Hargrove, E. Lee, R. Natter, S. Thompson, K. Weldon, and S. Yang, Tech. Dig. - Int. Electron Devices Meet. 11–14 December, 273 (1994).
[8]Y. Tamaki, S. Isomae, K. Sagara, and T. Kure, J. Electrochem. Soc. **135**, 726 (1988).
[9]L. Q. Xia, S. Nemani, M. Galiano, S. Pichai, S. Chandran, E. Yieh, D. Cote, R. Conti, D. Restaino, and D. Tobben, J. Electrochem. Soc. **146**, 1181 (1999).
[10]C. P. Chang, S. F. Shive, S. C. Kuehne, Y. Ma, H. Vuong, F. H. Baumann, M. Bude, E. J. Lloyd, C. S. Pai, M. A. Abdelgadi, R. Dail, C. T. Llu, K. P. Cheung, J. I. Colonell, W. Y. C. Lai, J. F. Miner, H. Vaidya, R. C. Liu, and J. T. Clemens, VLSI Technology Digest of Technical Papers, 1999 Symposium (unpublished), p. 161.
[11]S. Nag, Tech. Dig.-Int. Electron Devices Meet. 8–11 December, 841 (1996).
[12]M. Nandakumar, Tech. Dig.-Int. Electron Devices Meet. 7–10 December, 657 (1997).
[13]S. Lee, SSDM Dig. 524 (1997).
[14]K. Saino, K. Okonogi, S. Horiba, M. Sakao, M. Komuro, Y. Takaishi, T. Sakoh, K. Yoshida, and K. Koyama, Tech. Dig. - Int. Electron Devices Meet. 6–9 December, 149 (1998).
[15]G. Badenes, R. Rooyackers, E. Augendre, E. Vandamme, C. Perello, N. Heylen, J. Grillaert, and L. Deferm, J. Electrochem. Soc. **147**, 3827 (2000).
[16]Y. B. Park, J. Y. Kim, D. W. Seo, and W. G. Lee, J. Electrochem. Soc. **148**, G572 (2001).

Redistribution subject to AVS license or copyright; see http://scitation.aip.org/termsconditions. Download to IP: 140.113.38.11 On: Thu, 01 May 2014 05:24:40

[17] N. Balasubramanian and E. Johnson, J. Vac. Sci. Technol. B **18**, 700 (2000).
[18] H. Park, K. B. Kim, C. K. Hong, U. I. Chung, and M. Y. Lee, Jpn. J. Appl. Phys., Part 1 **37**, 5849 (1998).
[19] S. D. Kim, I. S. Hwang, H. M. Park, and J. K. Rhee, J. Vac. Sci. Technol. B **20**, 918 (2002).
[20] A. Itoh, M. Imai, and Y. Arimoto, Jpn. J. Appl. Phys., Part 1 **37**, 1697 (1998).
[21] J. Y. Cheng, T. F. Lei, and T. S. Chao, Jpn. J. Appl. Phys., Part 1 **36**, 1319 (1997).
[22] K. Shiozawa, T. Oishi, Y. Abe, and Y. Tokuda, Jpn. J. Appl. Phys., Part 1 **40**, 462 (2001).
[23] W. K. Yeh, T. Lin, C. Chen, J. W. Chou, and S. W. Sun, Jpn. J. Appl. Phys., Part 1 **38**, 2300 (1999).
[24] C. Chen, C. Y. Chang, J. W. Chou, W. Lur, and S. W. Sun, Jpn. J. Appl. Phys., Part 1 **39**, 1080 (2000).
[25] D. Ha, C. Cho, D. Shin, G. H. Koh, T. Y. Chung, and K. Kim, IEEE Trans. Electron Devices **46**, 940 (1999).
[26] H. Lee, J. M. Hwang, Y. J. Park, and H. S. Min, IEEE Electron Device Lett. **20**, 251 (1999).
[27] M. H. Park, S. H. Hong, S. J. Hong, T. Park, S. Song, J. H. Park, H. S. Kim, Y. G. Shin, H. K. Kang, and M. Y. Lee, Tech. Dig. - Int. Electron Devices Meet. 7–10 December, 669 (1997).
[28] J. W. Sleight, C. Lin, and G. J. Grula, IEEE Electron Device Lett. **20**, 248 (1999).
[29] P. Smeys, P. B. Griffin, Z. U. Rek, I. D. Wolf, and K. C. Saraswat, IEEE Trans. Electron Devices **46**, 1245 (1999).
[30] W. G. En, D. H. Ju, D. C. Chan, S. Chan, and O. Karlsson, *SOI Conference, 2001 IEEE International* (IEEE, New York, 2001), p. 85.
[31] H. Watanabe, K. Shimizu, Y. Takeuchi, and S. Aritome, Tech. Dig. - Int. Electron Devices Meet. 8–11 December, 833 (1996).
[32] P. Smeys, P. B. Griffin, Z. U. Rek, I. D. Wolf, and K. C. Saraswat, Tech. Dig. - Int. Electron Devices Meet. 8–11 December, 709 (1996).
[33] V. P. Gopinath, H. Puchner, and M. Mirabedini, IEEE Electron Device Lett. **23**, 312 (2002).
[34] C. Stuer, J. V. Landuyt, H. Bender, I. D. Wolf, R. Rooyackers, and G. Badenes, J. Electrochem. Soc. **148**, G597 (2001).
[35] T. K. Kim, D. H. Kim, J. K. Park, T. S. Park, Y. K. Park, H. J. Lee, K. Y. Lee, J. T. Kong, and J. W. Park, Tech. Dig. - Int. Electron Devices Meet. 6–9 December, 145 (1998).
[36] K. F. Dombrowski, A. Fischer, B. Dietrich, I. D. Wolf, H. Bender, S. Pochet, V. Simons, R. Rooyackers, G. Badenes, C. Stuer, and J. V. Landuyt, Tech. Dig. - Int. Electron Devices Meet. 5–8 December, 357 (1999).
[37] L. D. Landau and E. M. Lifschitz, *Theory of Elasticity* (Pergamon, Oxford, 1970).
[38] K. Kwok, E. Yieh, S. Robles, and B. C. Nguyen, J. Electrochem. Soc. **141**, 2172 (1994).

Redistribution subject to AVS license or copyright; see http://scitation.aip.org/termsconditions. Download to IP: 140.113.38.11 On: Thu, 01 May 2014 05:24:40